

# GeV emission of gamma-ray binary with pulsar scenario

HU XINGXING<sup>1</sup>★, TAKATA JUMPEI<sup>1</sup>† and TANG QINGWEN<sup>2</sup>‡

<sup>1</sup> Institute of particle Physics and astrophysics, School of Physics, Huazhong University of Science and Technology, Wuhan, Hubei, China

<sup>2</sup> Department of Physics, School of Sciences, Nanchang University, Nanchang 330031, China

10 April 2020

## ABSTRACT

We study GeV emission from gamma-ray binaries by assuming that the compact object is a young pulsar. We assume that the relativistic unshocked pulsar wind with Lorentz factor of  $10^{4-5}$  can produce the GeV emission by the inverse-Compton scattering process in the dense soft-photon field of the companion star. The travel distance of the unshocked pulsar wind that moves toward the observer depends on the orbital phase of the pulsar. We discuss that the orbital modulation of the GeV emission is a result of combination of the effects of the travel distance of the unshocked pulsar wind and of the anisotropic soft-photon field of the companion star. In this paper, we study how the effect of the travel distance of the unshocked pulsar wind affects to the orbital modulation of GeV emission. We apply our scenario to two gamma-ray binaries, LMC P3 and 4FGL J1405.5-6119. We find that with the suggested system parameters of LMC P3, the observed amplitude of the orbital modulation and the peak width are more consistent with the model light curve by taking into account the effect of the travel distance. For LMC P3, we analyze the GeV spectrum with 8-years *Fermi*-LAT data and discuss the broadband emission process in X-ray to TeV energy bands. We predict a possible system geometry for 4FGL J1405.5-6119 by fitting the GeV light curve.

**Key words:** shock waves, gamma-rays: stars, stars: massive stars: mass-loss, stars: neutron

## 1 INTRODUCTION

Gamma-ray binary is a system composed of a massive main-sequence star and a compact object (neutron star or black hole), and its non-thermal emission has a peak around 1 MeV in a  $\nu F_\nu$  of the spectral energy distribution (Dubus 2013). The multi-wavelength observations have confirmed about 10 gamma-ray binary systems, namely, PSR B1259-63/LS 2883 (Johnston et al. 1992; Cominsky 1994; Aharonian et al. 2005), PSR J2032+4127/MT91 213 (Lyne et al. 2015; Ho et al. 2017; Takata et al. 2017; Abeysekara et al. 2018), LS 5039 (Moldón et al. 2012; Takahashi et al. 2009; Aharonian et al. 2006; Abdo et al. 2009), LS I+61°303 (Albert et al. 2006; Aliu et al. 2013), 1FGL J1018.6-5856 (H. E. S. S. Collaboration et al. 2012; An et al. 2015), H.E.S.S. J0632+057 (Hinton et al. 2009; Li et al. 2017; Moritani et al. 2018), LMC P3 (Corbet et al. 2016), 4FGL J1405.4-6119 (Corbet et al. 2019) and HESS J1832-093 (Martí-Devesa & Reimer 2020; Tam et al. 2020). The gamma-ray binary is thought to be a short phase before high-mass X-ray binary in the binary evolution.

The gamma-ray binaries are probably divided into two groups based on the nature of the companion star, Be/Oe-type (PSR B1259-63/LS 2883, PSR J2032+4127/MT91 213, LS I+61°303

and H.E.S.S. J0632+057) or O-type (LS 5039, 1FGL J1018.6-5856, LMC P3 and 4FGL J1405.5-6119). The periods of gamma-ray binaries with the Be-type companion star ( $P_{orb} \sim$  several years, except for  $P_{orb} \sim 30$  days of LS I+61°303) is longer than that with the O-type companion star ( $P_{orb} \sim$  several days to about ten days). The orbit of the compact object moving around the Be-type companion star is elongated with an eccentricity  $e > 0.8$  (except for  $e \sim 0.6$  of LS I+61°303), while the eccentricity of the compact object circulating around the O-type companion star is  $e < 0.5$ . One interesting property of the emission from the gamma-ray binaries is that its observed intensity varies along the orbit. For the system with a Be-type companion star, the compact object will interact with the Be-disk twice in one orbit, and it has been observed that the emissions in X-ray and possibly in TeV bands are enhanced during the interaction (Chernyakova et al. 2009, 2015; Chen et al. 2019). A flare-like GeV emission from PSR B1259-63/LS 288 has been detected after the second interaction between the pulsar and Be-disk (Abdo et al. 2011; Tam et al. 2011, 2018). For the binary system with an O-type compact star, the X-ray/GeV and TeV bands would show an enhancement around the superior conjunction (SUPC) or inferior conjunction (INFC) of the orbit of the compact object and the GeV emission is observed over the entire orbit (Chang et al. 2016; Mariaud et al. 2015; Martí-Devesa & Reimer 2020).

Because of the recent discoveries of new gamma-ray binaries hosting O-type companion star (LMC LP3 and 4FG J1405.4-6119), the GeV emission properties of the binary systems have been re-

★ E-mail: huxx09791@hust.edu.cn

† E-mail: takata@hust.edu.cn

‡ E-mail: qwtang@ncu.edu.cn

vealed. The profile of LS 5039, for example, has a peak at the SUPC of the compact star's orbit (Abdo et al. 2009; Chang et al. 2016), while it of LMC P3 is shifted from the SUPC toward the periastron (Corbet et al. 2016; van Soelen et al. 2019); no orbital parameter except for the period is available for 4FG J1405.4-6119 (Corbet et al. 2019). The light curve of LS 5039 is described by a single broad peak, while LMC P3 will show an asymmetric pulse shape (see Figure 13), and 4FGL J1405.4-6119 probably shows a double peak structure (Figure 18). These properties of the light curve will provide an additional information of the GeV emission from the gamma-ray binaries hosting O-type companion star. Except for 1FGL J1018.6-5856, moreover, the peak position of the GeV emission of other three gamma-ray binaries is shifted from the peaks of the X-ray/TeV bands (Chang et al. 2016; Corbet et al. 2016, 2019) (no TeV observations for 4FGL J1405.4-6119 have been reported). This indicates that the GeV emission process are different from the processes of X-ray emission and TeV emission.

In this study, we discuss the model that the compact object of the gamma-ray binary is a young pulsar. In the pulsar scenario, the pulsar wind, which is composed of the electron/positron and magnetic field, interacts with the stellar wind/stellar disk. The X-ray and TeV emissions are produced by the synchrotron and inverse-Compton scattering process, respectively, of the relativistic pulsar wind particles accelerated at the termination shock (Tavani & Arons 1997). The orbital modulation of the emission in the X-ray bands attributes to the Doppler boosting effect due to the shocked pulsar wind (Dubus et al. 2010; Takata et al. 2014), and it in TeV bands is caused by the Doppler boosting effect plus the effects of the anisotropic photon field and of the pair-creation process.

The origin of the GeV emission from the gamma-ray binaries remains to be solved. It has been established that young pulsars emit the GeV gamma-rays in the magnetosphere (Abdo et al. 2009). However, the GeV emission modulating along the orbital phase of the gamma-ray binaries will not be explained by the magnetospheric emission. Within the framework of the pulsar binary system, the GeV emission modulating with the orbital phase would be produced by the Doppler boosting of the synchrotron photons due to the finite speed of the shocked pulsar wind (An & Romani 2017) or the inverse-Compton scattering (hereafter ICS) of the cold relativistic pulsar wind (Sierpowska-Bartosik & Torres 2008; Kapala et al. 2010; Torres 2011; Takata et al. 2014) or ICS the shocked pulsar wind (Yamaguchi & Takahara 2012; Zabalza et al. 2013) off the soft-photons from the companion star.

In this paper, we assume that the GeV emission of the gamma-ray binaries is produced by the ICS process between the cold-relativistic pulsar wind (hereafter unshocked pulsar wind) and the soft photon from the companion star. The orbital modulation of the ICS of the pulsar wind, especially for LS 5039 system, are discussed in the previous studies (Ball & Kirk 2000; Zabalza et al. 2013; Takata et al. 2014). Since the soft photon field is anisotropic in the emission region and depends on the distance from the companion star to the emission region, the emissivity of ICS varies along the orbital phase. For the circular orbit, for example, the ICS intensity tends to be the maximum value at the SUPC and the minimum at the INFC, since the scattering processes at SUPC and INFC are caused by a head-on collision process and a tail-on collision process, respectively. For an elongated orbit, since the soft-photon density on the orbit of the pulsar is maximum at the periastron, the orbital position of the intensity maxima would shift toward the periastron. In the previous studies, however, the predicted light curve has a single peak in the light curve and does not discuss the for-

mation of the double peaks. An additional effect, therefore, will be required to explain the orbital variation of the GeV emissions of LMC LP3 and especially for 4FG J1405.4-6111.

In addition to the effect of the anisotropic soft-photon field, we will explore the orbital modulation caused by the dependency of travel distance of the unshocked pulsar wind that moves toward the observer on the orbital phase. This effect is introduced in Sierpowska-Bartosik & Bednarek (2008) for PSR B1259-63/SS2883 system and in Sierpowska-Bartosik & Torres (2008); Khangulyan et al. (2008) for the very high-energy emission (TeV emission) of LS 5039. Since the interaction between the pulsar wind and stellar wind/disk will produce a termination-shock with cone-like structure (Canto et al. 1996), the distance from the pulsar to the termination-shock ( $r_s$  in Figure 2) increases with the angle measured from the axis created by the pulsar and the companion star. This causes a dependency of the distance from the pulsar to the termination shock in the direction of the observer on the orbital phase and results in the orbital dependent intensity of the ICS of the unshocked pulsar wind. For the gamma-ray binary with O-type star, the GeV light curve is not well studied with the effect of the shock geometry and the system parameters. In this paper, therefore, we will perform an investigation for the modulation of the GeV emission with the shock-cone model, and will apply the model to two gamma-ray binaries, LMC P3 and 4FGL J1405.4-6119.

LMC P3 is the first gamma-ray binary outside Milky Way and it is discovered in the Large Magellanic Cloud (LMC) (Corbet et al. 2016), which is a neighbor galaxy located at about 50 kpc from the Earth (Macri et al. 2006; Pietrzyński et al. 2013; de Grijs et al. 2014). The companion star in the LMC P3 system is O-type star, but the compact object has not been identified yet. In the LMC,  $\sim 50$  supernova remnants (SNRs) are known to emit X-rays (Seward et al. 2012), and LMC P3 is associated with SNR 0535-67.5 in the H II region DEM L241 (Davies et al. 1976). Long et al. (1981) reports the first detection of the X-ray emission from the SNR 0535-67.5. Seward et al. (2012) find a compact X-ray source (CXOU J053600.0-673507) with a luminosity of  $\sim 2 - 3 \times 10^{35} \text{ erg s}^{-1}$  in 0.3-10keV energy bands and an optical counterpart, O5III(f) star. They therefore suggest that CXOU J053600.0-673507 is the high-mass X-ray binary hosting neutron star or black hole. Corbet et al. (2016) analyze the GeV counter part (LMC P3) of CXOU J053600.0-673507 in data of *Fermi* Large Area Telescope (*Fermi*-LAT) and find a 10.3 day periodic modulation that reveals LMC P3/CXOU J053600.0-673507 is the binary system with a orbital period of  $P_{orb} \sim 10.3$  day. They also confirm the orbital modulation of the X-ray emission. HESS Collaboration et al. (2018) subsequently detect the TeV emission from LMC P3. van Soelen et al. (2019) find that the binary system is slightly eccentric with an eccentricity  $e = 0.40 \pm 0.07$  and that the mass function,  $f = 0.0010 \pm 0.0004 M_{\odot}$ , favors a neutron star as a compact object. These multi-wavelength observations will suggest that LMC P3/CXOU J053600.0-673507 is the gamma-ray binary system hosting an energetic young pulsar. The orbital parameters determined by van Soelen et al. (2019) suggest that the GeV emission has a peak intensity at a phase between the superior conjunction and periastron, while TeV emission (and probably X-ray emission) shows the maximum intensity at around the inferior conjunction.

4FGL J1405.1-6119 is the recently discovered gamma-ray binary with an orbital period of  $P_{orb} \sim 13.7135$  days (Corbet et al. 2019) and is hosting O6.5 III companion star. The estimated distance with using tabulated absolute magnitude for an O6.5 III star is  $d \sim 6.4 - 8.9 \text{ kpc}$  (Corbet et al. 2019). The GeV light

curve is composed of a strong narrow peak plus a small peak. Corbet et al. (2019) reveal that the X-ray emission (CXOGSG J140514.4-611827) also modulates with the orbital phase. The position of the main peak of the GeV emission is shifted from the X-ray peak that would be described by a single broad peak. In this paper, since the orbital parameters have not been reported, we predict a possible geometry of the binary system by fitting GeV light curve with the model.

In this paper, we will discuss the multi-wavelength emission properties. Ackermann et al. (2016) report the GeV spectrum of LMC P3 with six years of *Fermi*-LAT observations. We also redo the spectral analysis of LMC P3 with the eight years of the *Fermi*-LAT observations, since the spectral information in the GeV bands is important to understand the multi-wavelength emission process from X-ray to TeV energy bands. In section 2, we extract the GeV spectrum of LMC P3 using *Fermi*-LAT data. In section 3, we will describe our theoretical model for the GeV emissions from the unshocked pulsar wind and X-ray/TeV emissions from the shocked pulsar wind. We discuss the dependency of the GeV light curve with the system parameters and compare the results with the observations for LMC P3 and 4FGL J1405.1-6119 in section 4. A brief summary will be provided in section 5.

## 2 FERMI DATA ANALYSIS

### 2.1 Event Selections and Background Subtraction

Gamma-ray events for LMC (RA.=80.894, Decl.=−69.756) are derived from the *Fermi* Science Support Center<sup>1</sup>, which span the period from 4th Aug 2008 to 4th Aug 2016. Due to low background contamination, we cut the low-energy events, such as below 200 MeV, and select them up to 100 GeV, which lead to a  $10^\circ \times 10^\circ$  box region (ROI) being suited in this gamma-ray band. Events with zenith angles  $>90^\circ$  are excluded to eliminate the contamination from the Earth-limb gamma rays. Instrument response function (IRSF) of P8R2\_SOURCE\_V6 is employed in our data analysis.

As discussed in Tang et al. (2017) and Tang (2018), the G template, which includes four gaussian-disk sources and four point sources, is a good template for recovering the gamma rays observed by *Fermi*-LAT in LMC field. In the G template, LMC P3 is near the centre of the G template (RA.=80.894, Decl.=−69.756). For source of LMC P3, other 7 sources of the G template (G1, G2, G3, G4, P1, P2 and P4) and 3 point sources (3FGL J0601-7036, 3FGL J0529-7242 and 3FGL J0437-7330) are the background sources with spectral parameters free, while 3FGL sources, that are out of ROI but  $15^\circ$  around LMC centre, are the buffering background sources with all spectral parameters fixed. In addition, a Galactic diffuse source and an isotropic gamma-ray source are added, which are represented by “gll\_iem\_v06.fits” and “iso\_P8R2\_SOURCE\_V6\_v06.txt” respectively.

### 2.2 Spectral analysis for LMC P3

Gamma-rays between 200 MeV and 100 GeV are divided into 11 logarithmic energy bins. A single power-law spectrum (PL) is assumed for LMC P3, while all background sources are modeled by corresponding spectral functions in Ackermann et al. (2016) & Tang et al. (2017), i.e., PL for 5 LMC sources (G2, G3, G4, P2

and P4), power law with exponential cutoff (PLC) for the P1, log-parabola (LP) for the G1. A global fit is performed in a python package (Fermipy)<sup>2</sup>(Wood et al. 2017), whose resultant parameters are fixed in the afterward spectral data fits except for the normalization of the LMC P3. Performing the binned maximum-likelihood analysis, we report the flux value and the upper-limit flux (95% C.L.), which are plotted in Fig. 17. Our results are consistent with that reported in Ackermann et al. (2016).

## 3 THEORETICAL MODEL

In our theoretical model, we assume that the compact object is a pulsar, which produces strong pulsar wind interacting with the stellar wind (Figure 1). The unshocked pulsar wind scatters off the soft photons from the companion star and produces GeV emission that modulates along the orbital phase. The interaction between the relativistic pulsar wind and the stellar wind creates the termination shock. At the termination shock, the pulsar wind particles (electrons and positrons) are accelerated to higher energy and produce the X-ray and TeV gamma-ray via the synchrotron and the ICS process, respectively.

### 3.1 Emission from unshocked pulsar wind

We assume that (i) the unshocked pulsar wind is isotropic, (ii) it is composed of the electron/positron and magnetic field and (iii) it carries the spin-down power ( $L_{sd}$ ) of the pulsar. To describe the particle energy of the pulsar wind, we introduce so called magnetization parameter that is the ratio of the magnetic energy to the particle energy of the relativistic wind,

$$\sigma(r) = \frac{B_W^2(r)}{4\pi\Gamma_W(r)u_W(r)n_W(r)m_e c^2}, \quad (1)$$

where  $B_W$  is the magnetic field in the wind region before the shock,  $n_W$  is the proper number density of the electrons/positrons,  $u_W$  and  $\Gamma_W = \sqrt{1 + u_W^2}$  are the dimensionless radial four velocity and the Lorentz factor of the unshocked flow, respectively,

Using the conservations of the particles and of the energy, we may relate the Lorentz factor of the relativist flow ( $u_W \sim \Gamma_W$ ) with the magnetization parameter as described in (Kennel & Coroniti 1984a)

$$\begin{aligned} \Gamma_W(r) &= \frac{L_{sd}}{4\pi n_W(R_{lc})m_e c^3 R_{lc}^2 (1 + \sigma)} \\ &\sim 3 \times 10^4 (1 + \sigma)^{-1} \left( \frac{\kappa}{10^5} \right)^{-1} \left( \frac{L_{sd}}{10^{37} \text{ erg s}^{-1}} \right)^{1/2}, \end{aligned} \quad (2)$$

where  $R_{lc}$  is the light cylinder radius of the pulsar and  $\Gamma_W n_W(R_{lc}) = \kappa N_{GJ}(R_{lc})$  with  $N_{GJ}(R_{lc}) = B(R_{lc})/(2\pi R_{lc}e)$  being the Goldreich-Julian number density measured at the light cylinder and  $\kappa$  the multiplicity. The multiplicity is the number of new positron/electron pairs that a primary particle can make via pair-creation cascade. The multiplicity of the young pulsars will be determined by the pair-creation cascade above the polar cap acceleration and it will not exceed  $\sim a \text{ few } \times 10^5$  (Timokhin & Harding 2015, 2019; Hibsman & Arons 2001a,b). We expect therefore that the typical Lorentz factor of the unshocked pulsar wind will be of the order of  $10^{4-5}$ . In this paper, we assume that the energy conversion from

<sup>1</sup> <https://fermi.gsfc.nasa.gov/ssc/>

<sup>2</sup> <https://fermipy.readthedocs.io/en/stable>



the magnetic energy to the particle energy is almost completed at vicinity of the pulsar and produces an kinetic energy dominated flow,  $\sigma \ll 1$ .

In this study, we assume that the particles in the unshocked pulsar wind have a mono-energetic distribution. If the pair-creation cascade is developed in the pulsar wind, the energy distribution will be modified (Sierpowska-Bartosik & Torres 2008). In the current study, however, the unshocked pulsar wind has a Lorentz factor of the order of  $10^{4-5}$  and produce GeV photons via the ICS process. Since the optical depth of GeV photons is much less than unity, the pair-creation cascade will not develop in the pulsar wind region.

The radiation power per unit energy per unit solid angle of single particle is calculated from

$$\frac{dP_{IC}}{d\Omega} = \mathcal{D}^2 \int_0^{\theta_c} (1 - \beta_W \cos \theta_0) I_b / h \frac{d\sigma'}{d\Omega'} \cos \theta d\Omega_0, \quad (3)$$

$$I_b = \frac{2\epsilon^3 / h^2 c^2}{\exp(\epsilon/kT) - 1} \quad (4)$$

where  $\mathcal{D} = \Gamma_w^{-1}(1 - \beta_W \cos \theta_s)$ ,  $\beta_W$  is the wind speed in units of the speed of light,  $\theta_0$  (or  $\theta_s$ ) describes the angle between the direction of the particle motion and the propagating direction of the incident (or scattered) photon and  $\theta_c$  is the angular size of the companion star measured from the emission region. In addition,  $h$  is the Planck constant,  $I_b$  is the distribution of background photons, and  $d\sigma'/d\Omega'$  represents the differential Klein-Nishina cross section.

Total power radiated toward the observer by the unshocked pulsar wind is calculated from

$$P_{IC} = \int \int \frac{dP_{IC}}{d\Omega} \Gamma_w(r) n_W(r) r^2 d\Omega dr, \quad (5)$$

where the integration for the distance is taken from the vicinity of the pulsar to the shock in the direction of the observer. The modulation of the emission with the orbital phase is produced by (i) anisotropy of the soft photon at the emission region and (ii) the dependence of the distance from the pulsar to the termination shock in the direction of the observer on the orbital phase (Sierpowska-Bartosik & Torres 2007). To calculate the travel distance of the unshocked pulsar wind, we explore the shock cone geometry discussed in Canto et al. (1996) (Figure 2),

$$r_s(\theta) = D \sin \theta \csc(\theta + \theta_1) \quad (6)$$

and

$$\theta_1 \cot \theta_1 = 1 + \eta(\theta \cot \theta - 1), \quad (7)$$

where  $D = \frac{0.35 \text{ AU}(1-e^2)}{1+e \cos \phi}$  is the separation between two stars,  $\theta$  and  $\theta_1$  describe the angle to a position on the shock measured from the pulsar and companion star, respectively (c.f. Figure 2). In addition,  $\eta$  is the ratio of the momenta of the two winds,

$$\eta \equiv \frac{L_{sd}}{\dot{M} v_w c}, \quad (8)$$

where  $\dot{M}$  is the mass loss rate of the outflow from the companion star and  $v_w$  is the speed of the outflow. Puls et al. (1996) study the mass loss rate of O-type star by fitting the  $H\alpha$  profile. They find that the mass loss rate can be larger than  $10^{-6} M_\odot \text{ year}^{-1}$ , and the terminal wind velocity is around 2000 km/s, for which the momentum ratio  $\eta$  can be in the order of 0.01 for a spin down pulsar of the pulsar  $L_{sd} \sim 10^{36} \text{ erg s}^{-1}$ .

Figure 3 and 4 summarize the travel distance of the unshocked pulsar wind toward the observer as a function of the orbital phase

for the different system parameters. In Figure 3, we present the results with  $\eta = 0.03$  and system inclination angle  $\alpha = 30^\circ$ ; the dotted line and solid line are results for the eccentricity  $e = 0$  and  $e = 0.4$ , respectively: For circular orbit (dashed line), since the separation is constant, no periastron is defined, while for eccentricity of 0.4 (solid line), we set the periastron to be phase 0. In the figure, we choose the phase zero ( $\Phi_{orb} = 0$ ) as the periastron for elongated orbit and  $\Phi_{orb} = 0.24$  as the INFC. With  $\Phi_{orb} = 0.24$  of the INFC, the superior conjunction is located at  $\Phi_{orb} = 0.76$  for the orbit with  $e = 0$  and  $\Phi_{orb} \sim 0.98$  for  $e = 0.4$ , respectively. The unshocked pulsar wind travels toward the observer is stopped if the line of sight is outside the shock cone. In such a case, the travel distance of the unshocked pulsar wind moving toward the line of sight has a finite value for whole orbital phase, as Figure 3 shows. As we expect for the case of  $\alpha > 90^\circ - \theta_{shock}$ , the line of sight at around the INFC is within the shock cone and the pulsar wind moving toward the observer will not be stopped by the shock. We note that if there is a back shock proposed by Bosch-Ramon et al. (2012), the pulsar wind in all direction would be stopped by the vicinity of the pulsar. In this paper, however, we do not consider such effect of the back shock.

In Figure 3, we can see that the maximum and minimum travel distances are located at around the INFC and SUPC, respectively. For eccentric binary system (solid line in Figure 3), we can see that the position of the maximum travel distance slightly shifts from INFC toward the apastron. This is because the distance between two stars,  $D$ , changes along the orbital phase. Figure 3 also indicates that since the variation of travel distance along the orbit becomes larger for the orbit with a larger eccentricity, the effect of the travel distance on the orbital modulation becomes larger for the binary system with more elongated orbit. In Figure 4, we can see that the amplitude of the variation of the travel distance along the orbit increases with increasing of the momentum ratio, implying the effect could be more important for the binary system with a stronger pulsar wind. Actually, the effect of the travel distance will compensate with the effect of the anisotropic field of the soft photon field of the ICS process, as we will discuss in later.

### 3.2 Emission from the shocked pulsar wind.

At the shock, the kinetic energy of the pulsar wind before the shock is converted into the internal energy of the shocked pulsar wind. To evaluate the physical quantities of the pulsar wind just after the shock, we apply the results of the perpendicular MHD shock (Kennel & Coroniti 1984a,b). The current approximation of the perpendicular shock would be valid for the emission happen only around the apex of the shock ( $r \sim r_s$ ). A more realistic treatment would be more complicated, since the shock jump conditions depends on the inclination of the magnetic field relative to the shock surface and, the inclination varies with position of the shock region. In our model, however, the structure of the emission from the shock region are mainly originated around the apex. Hence, the current treatment could provide a good assumption to discuss the high-energy emission from the system. For the pulsar wind flow dominated by the particle kinetic energy, that is, low  $\sigma$  limit ( $\sigma \ll 1$ ), the radial four velocity  $u = \sqrt{\Gamma^2 - 1}$  where  $\Gamma$  is Lorentz factor of flow, proper number density, and magnetic field strength are expressed as

$$u_2 = \left( \frac{1 + 9\sigma}{8} \right)^{1/2} \quad (9)$$

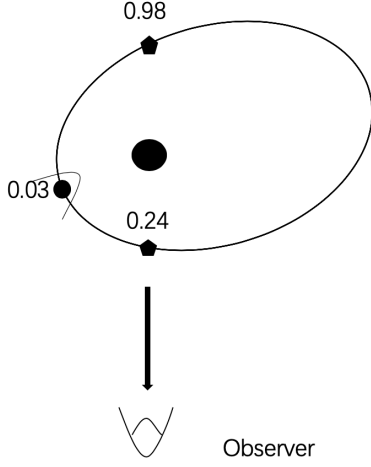


**Figure 1.** Schematic view for LMC P3. The pulsar is orbiting around the companion star (large filled circle) with an eccentricity of  $e = 0.4$ . An interaction of the pulsar wind and stellar wind creates a shock, which wraps the pulsar. In section 4.2, we assume that the orbital phases  $\phi=0.03, 0.24$  and  $0.98$  corresponds to the periastron, INFC and SUPC, respectively, of the pulsar orbits, where the phase zero refers the time MJD 57,410.25. [van Soelen et al. 2019](#). This orbital parameters are chosen to explain the observed GeV modulation with the inverse-Compton process of the cold-relativistic pulsar wind.

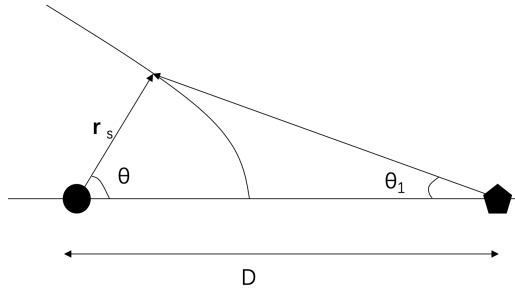


**Figure 2.** Geometry of the shock cone. The black filled circles and regular pentagon represent the pulsar and the companion star, respectively. The distance from the pulsar to the shock,  $r_s$ , is described by the equation (6).

$$n_2 = \frac{n_1 u_1}{u_2} \quad (10)$$

and

$$B_2 = 3B_1(1 - 4\sigma), \quad (11)$$

respectively. Here the subscript 1 and 2 represent the physical quantities just before and after the shock, respectively. The number density and magnetic field strength just before the shock are calculated

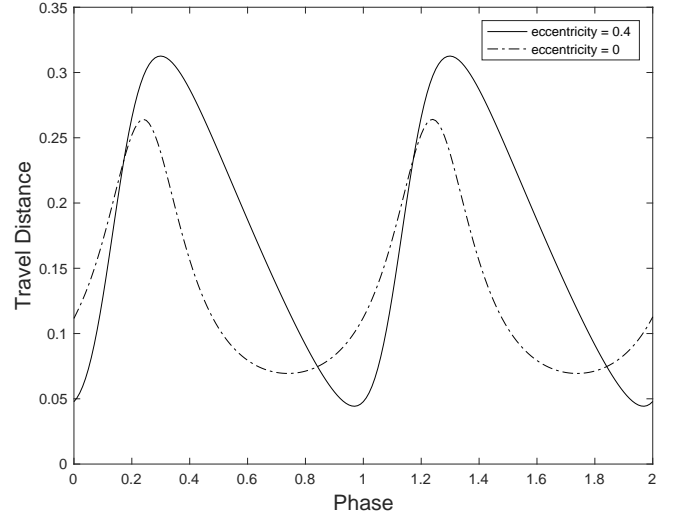


**Figure 3.** Variation of the travel distance of the unshocked pulsar wind before the shock. The geometry of the shock cone is modeled by [Canto et al. 1996](#). The results are for  $\eta = 0.03$  and inclination angle is  $\alpha = 30^\circ$ . The dotted line and solid line are for the eccentricity  $e = 0$  and  $e = 0.4$ , respectively. The periastron and INFC is located at  $\Phi_{peri} = 0$  and  $\Phi_{INFC} = 0.24$ , respectively. The SUPC is located at  $\Phi_{SUPC} = 0.76$  for  $e = 0$  and  $\Phi_{SUPC} = 0.98$  for  $e = 0.4$ , respectively.

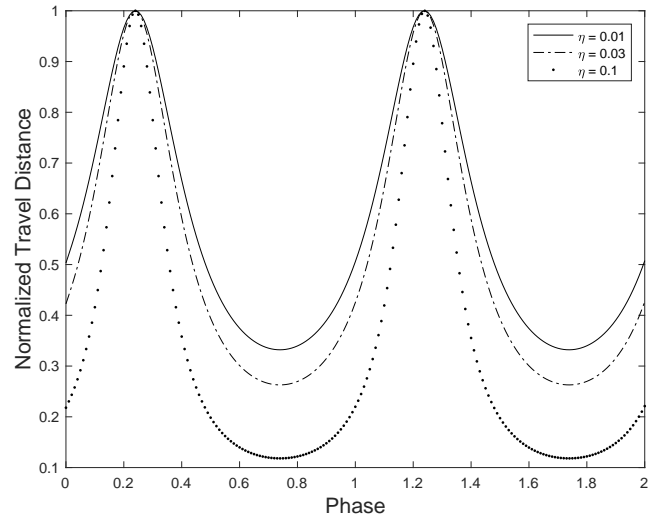


**Figure 4.** Variation of the travel distance of unshocked pulsar wind with using the circular orbit  $e = 0$  and the inclination angle  $\alpha = 30^\circ$ . The travel distance is normalized by the value at the INFC. The results are for the moment ratio  $\eta=0.01$  (solid line),  $0.03$  (dash-dotted line) and  $0.1$  (dotted line), respectively. The physical distance at the INFC is  $\sim 0.13\text{AU}$  for  $\eta = 0.01$ ,  $\sim 0.26\text{AU}$  for  $\eta = 0.03$  and  $\sim 1.0\text{AU}$  for  $\eta \sim 0.1$ .

from

$$n_1 = \frac{\dot{E}_{sp}}{4\pi u_1 \Gamma_1 r_s^2 m_e c^3 (1 + \sigma)}, \quad (12)$$

and

$$B_1 = \sqrt{\frac{E_{sp} \sigma}{r_s^2 c (1 + \sigma)}}, \quad (13)$$

respectively, where  $\Gamma_1 = \Gamma_w$  and  $r_s$  is the distance to the shock from the pulsar.

For the down stream flow, the number density and magnetic field is calculated from the conservations that

$$n(r)u(r)r^2 = \text{constant} \quad (14)$$

$$u(r)B(r)r/\Gamma_{sw} = \text{constant} \quad (15)$$

where  $r$  is the distance from the shock and  $\Gamma_{sw}$  is the Lorentz factor of the shocked wind. In this paper, the four velocity  $u(r)$  is assumed to be a constant about 0.4 along the flow, that is,  $\Gamma_{sw} \sim 1.08$ , which is chosen to explain the orbital modulation of the observed X-ray emission. Here we assume that the Lorentz factor of post-shocked flow is constant. In [Bogovalov et al. \(2008\)](#) and their subsequent studies ([Bogovalov et al. 2019](#)), they show that the post-shocked flow accelerates at the region far-from the apex ( $r \gg r_s$ ), because of the adiabatic expansion. So our assumption of the constant speed may not be adequate except for around the apex. Based on our calculation, on the other hand, we would say that most of the emission from the shocked region is coming from the region around apex, where the magnetic field is stronger and the soft-photon energy density is larger. Therefore, the power of the emission far from the apex is much smaller than that around the apex. Hence the current assumption may be good enough.

We assume the initial distribution of the shocked particles follows a power law form,

$$f_2(\gamma) \propto \gamma^{-p}, \quad \gamma_{\min} \leq \gamma \leq \gamma_{\max} \quad (16)$$

and the normalization factor is determined from

$$n_2 = \int_{\gamma_{\min}}^{\gamma_{\max}} f_2(\gamma) d\gamma. \quad (17)$$

The maximum Lorentz factor is determined by  $\min(\gamma_g, \gamma_{syn})$ , where  $\gamma_g$  is the Lorentz factor whose gyration radius is equal to the shock distance, and  $\gamma_{syn}$  is the Lorentz factor at which acceleration timescale is equal to the synchrotron cooling timescale,  $\tau_{ac} = \tau_{syn}$ , where  $\tau_{ac} = \gamma m_e c / Be$  and  $\tau_{syn} = 9m_e^3 c^5 / e^4 B^2 \gamma$ , respectively. We assume  $\gamma_{\min} = 4 \times 10^5$  to explain the broadband spectrum.

The particles will loose their energy owing to the cooling processes; adiabatic expansion, synchrotron emission, and IC scattering. We calculate the evolution of the Lorentz factor from

$$\frac{d\gamma}{dt} = \frac{\gamma}{3n} \frac{dn}{dt} - \left( \frac{d\gamma}{dt} \right)_{syn} - \left( \frac{d\gamma}{dt} \right)_{IC}, \quad (18)$$

where the first term represents the adiabatic expansion cooling. The synchrotron and ICS cooling processes are calculated from

$$\left( \frac{d\gamma}{dt} \right)_{syn} = \frac{4e^4 B^2 \gamma^2}{9m_e^3 c^5} \quad (19)$$

and

$$\left( \frac{d\gamma}{dt} \right)_{IC} = \int \int (E - E_s) \frac{\sigma_{ICC}}{m_e c^2 E_s} \frac{dN_s}{dE_s} dE_s dE, \quad (20)$$

respectively. Figure 5 summarizes the timescale of the cooling processes at the periastron (with the orbital parameters in Tables 1 and 2) as a function of the Lorentz factor.

From the number conservation in the phase space, the distribution function at the distance  $r$  can be calculated from

$$f(r, \gamma) = \frac{n}{n_2} f_2 \frac{d\gamma_2}{d\gamma}, \quad (21)$$

where the subscript 2 represents the initial value.

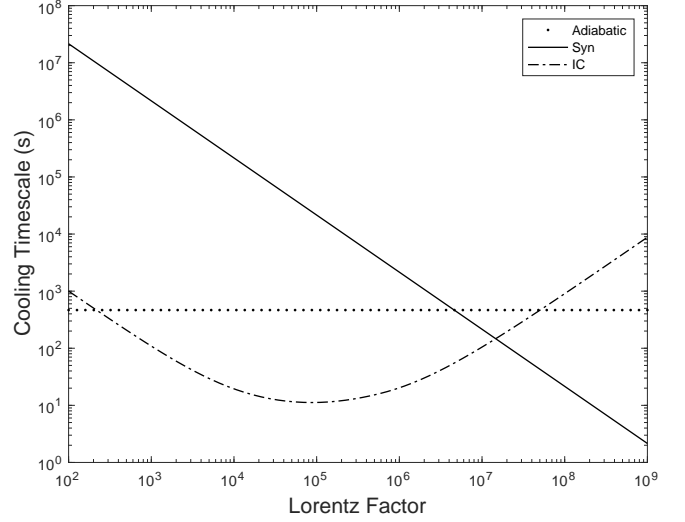


**Figure 5.** Cooling timescale at the periastron with the orbital parameters in Table 2. At the periastron, the separation of two stars is  $D = 0.25\text{AU}$  and the magnetic field at the shock is about 0.6 Gauss.

We calculate the ICS process of single particle with equation (3). For the synchrotron radiation, the radiation power per unit energy is calculated from

$$P_{syn} = \frac{\sqrt{3}e^3 B \sin \theta_p}{hm_e c^2} F\left(\frac{E}{E_c}\right) \quad (22)$$

$E_c = 3\hbar e \gamma^2 B \sin \theta_p / 4\pi m_e c$  is typical photon energy,  $\theta_p$  is the pitch angle and  $F(x) = x \int_0^\infty K_{5/3}(y) dy$ , and  $K_{5/3}$  is the modified Bessel function. For the pitch angle, we use the averaged value,  $\sin^2 \theta_p = 2/3$ .

The Doppler boosting effect due to the finite speed of the post shocked flow enhances or suppresses the observed emission and can cause an orbital modulation of the emission ([Dubus et al. 2010](#); [Takata et al. 2014](#)). The Doppler factor is calculated from

$$D_{obs} = \frac{1}{\Gamma_{sw}(1 - \beta_{sw} \mathbf{e}_{obs} \cdot \mathbf{e}_{flow})} \quad (23)$$

where  $\beta_{sw}$  is the speed of the shocked pulsar wind in units of the speed of light,  $\mathbf{e}_{flow}$  is the unit vector along the direction of the flow and  $\mathbf{e}_{obs}$  is the unit vector in the direction of the observer. To calculate the angle between the flow direction and observer direction, we approximate that the flow is in the orbital plane and moves away from the companion star, since the stellar wind pressure dominates the pulsar wind pressure ( $\eta \ll 1$ ). The observed photon energy and flux are modified as  $\epsilon = D_{obs} \epsilon'$  and  $F_v(\epsilon) = D_{obs}^3 F'_v(\epsilon')$ , where the primed quantities refer to the value in the co-moving frame.

Finally, the pair-creation process between the high-energy gamma-ray and the soft-photon from the companion star may affect to the observed TeV emission. We calculate the optical depth of the pair-creation process from ([Gould & Schröder 1967](#))

$$\tau_{\gamma\gamma} = \int_0^l dl \int_{4\pi} d\Omega (1 - \mu) \int_{\frac{2}{\epsilon\gamma(1-\mu)}}^\infty d\epsilon n_{ph}(\epsilon, \Omega) \sigma_{\gamma\gamma} \quad (24)$$

where  $l$  is the distance over which the  $\gamma$ -ray photon travels,  $\mu = \cos \theta$ ,  $d\Omega = d\mu d\phi$ , and  $n_{ph}(\epsilon, \Omega)$  is the number density of the low-energy target photons. The cross section of the process is given as

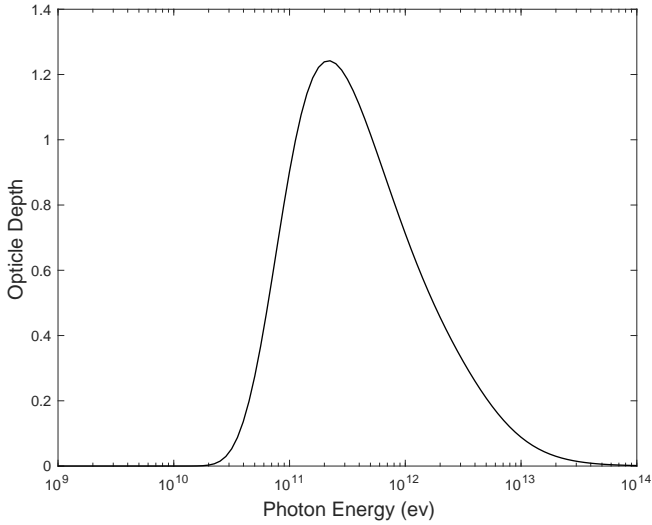


**Figure 6.** Optical depth along the line of sight of the photon-photon pair-creation process at the periastron of the binary orbit with the system inclination angle  $\alpha = 30^\circ$  and eccentricity  $e = 0.4$ .

(Jauch & Rohrlich 1976),

$$\sigma_{\gamma\gamma} = \frac{3}{16} \sigma_T (1 - \beta^2) \left[ (1 - \beta^4) \ln \left( \frac{1 - \beta}{1 + \beta} \right) - 2\beta(2 - \beta^2) \right] \quad (25)$$

where

$$\beta = \sqrt{1 - \frac{1}{\epsilon \epsilon_\gamma (1 - \mu)}} \quad (26)$$

and  $\sigma_T$  is the Thomson cross section. Figure 6 shows the optical depth of the photon traveling toward the observer at periastron. For the photons with an energy less than  $10^{10}$  eV, the pair-creation process is negligible, as shown in the figure.

## 4 RESULT

In this section, first we will discuss on the GeV emission within the framework of the ICS model of the unshocked pulsar wind and discuss the dependency of the shape of the light curve on the system parameters. Then, we will compare the model light curve with the Fermi-LAT observation of the gamma-ray binary LMC P3. We compare the predicted X-ray and TeV-emissions from the shocked pulsar wind with the observations for LMC P3. We discuss the system geometry of 4FGL J1405.4-6119 by fitting the observed GeV light curve.

### 4.1 ICS emission from unshocked pulsar wind

We assume that the GeV emission from the gamma-ray binary is produced via ICS process of the unshocked pulsar wind and assume that the particles in the unshocked pulsar wind have a mono-energetic distribution (in this paper, we assume the Lorentz factor to be  $3 \times 10^4$ , c.f. equation (2)). In section 3.1, we discussed a detailed of the calculation method. The variability of the emissivity of ICS process along the orbital phase is mainly determined by the variability of three effects, namely, (i) the size of the emission region, (ii) collision angle between the pulsar wind and soft-photon from the companion star, and (iii) soft photon and the den-

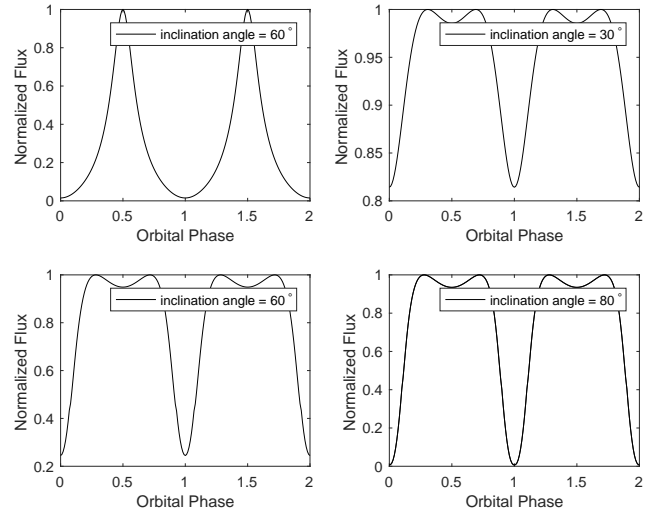


**Figure 7.** Dependency of the orbital modulation of ICS emission from unshocked pulsar wind with the system inclination angle. The result is for the circular orbit and  $\eta = 0.03$ . In the top left panel, the orbital modulation by assuming the constant travel distance of the pulsar wind is presented for the comparison. The INFC and SUPC happen  $\Phi_{INFC} = 0$  and  $\Phi_{SUPC} = 0.5$ , respectively

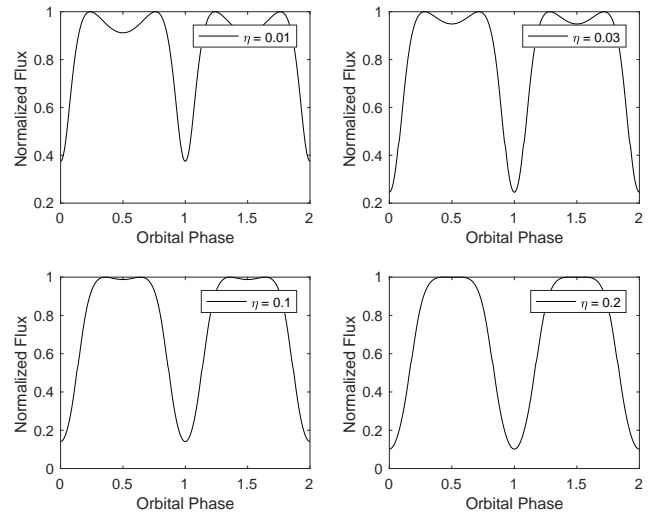


**Figure 8.** Dependency of the orbital modulation of ICS emission from unshocked pulsar wind with the momentum ratio of two winds. The result is for the circular orbit and the system inclination angle  $\alpha = 60^\circ$ . The INFC and SUPC happen at  $\Phi_{INFC} = 0$  and  $\Phi_{SUPC} = 0.5$ , respectively

sity of background photon. These parameters then tightly relate to the system parameters, momentum ratio of the two winds, inclination angle of the system, eccentricity, and the true anomaly of the INFC/SUPC measure from the periastron. In this section, therefore, we investigate how orbital variation depends on the system parameters.

Firstly, Figure 7 summarizes how the inclination angle of the system affects to the light curve by using the circular orbit. For the circular orbit, since the distance to the apex of the shock from the pulsar is constant with the orbital phase, the soft photon density at the unshocked pulsar wind region is also almost constant. Hence, the orbital variation is mainly caused by the effects of the collision angle and the travel length, which depends on the inclination

**Table 1.** Parameters of the pulsar and O star applied in this study.

Spin-down power $L_{sp}$	Magnetization parameter $\sigma$	O star radius $R_c$	O star temperature $T_c$	Wind momentum ratio $\eta$
$6 \cdot 10^{36}$ erg/s	0.003	$14.5 R_\odot$	$2.5 \cdot 10^4$ K	0.01

**Table 2.** Parameters of the systems applied in Figure 13.

Orbital period	Eccentricity	Inclination angle	Periastron	INFC	SUPC
10.3 days	0.4	$30^\circ$	0.03	0.24	0.98

angle of the system. In Figure 7, we set the momentum ratio to be  $\eta = 0.03$  and, the INFC and SUPC happen at  $\Phi_{INF} = 0$  and  $\Phi_{SUPC} = 0.5$ , respectively. The top-right, bottom-left and bottom-right panels show the result for  $\alpha = 30^\circ$ ,  $60^\circ$  and  $80^\circ$ , respectively. In the top left column, we present the orbital modulation with  $\alpha = 60^\circ$  by assuming the constant travel distance of unshocked pulsar wind for the comparison (i.e., the orbital modulation is only affected by the variation of the collision angle). For a constant travel length with the orbital phase, the observed flux acquire the maximum value at the SUPC and the minimum value at the INFC, since the collision angle is the maximum (head-on) and minimum (tail-on) at the SUPC and INFC, respectively.

As Figure 7 shows, we find that the overall feature of the light curve does not change, even the effect of the travel distance is taken into account. However we find that the light curve has a small dip at SUPC. This is because the shortest travel distance occurs at SUPC, as discussed in section 3. By the comparing the light curves between top-left and bottom-left panels for  $\alpha = 60^\circ$ , we can find that the effect of the travel length (i) reduces the amplitude of the orbital variation and (ii) makes the width of the peak wider. By comparing among top right, bottom-left and bottom-right panels, we see that as the inclination angle increases, the amplitude of variation becomes larger. This suggests that the effect of travel length become more significant for a smaller inclination angle.

In Figure 8, we summarize the dependency of the momentum ratio  $\eta (= L_{sd}/(\dot{M}v_{wc}))$  for the circular orbit  $e = 0$ . The momentum ratio affects to the variation of the observed flux, since it affects to (i) the travel length of the unshocked pulsar wind (c.f. Figure 4) and (ii) the density soft-photon field at the emission region. For example, Figure 4 shows that for larger momentum ratio, the ratio of the travel distance at the SUPC to one at the INFC is smaller, and therefore the dip at SUPC tends to be dipper. The second effect about the soft photon density is caused because for the larger momentum ratio, the apex of the shock is located at the position closer to the companion star, and the soft photon number density of the emission region become larger. This effect tends to increase the emissivity at around the SUPC, since the pulsar wind approaching toward the companion star produces the observed emission at around the SUPC. From Figure 8, we find that the dip at the SUPC becomes shallow with increase of the momentum ratio (stronger pulsar wind). This is because the second effect of the photon density overcomes the first effect of the travel length. The current calculation suggests therefore that the effect of the travel distance is more important for the binary system in which the stellar wind is much stronger than that of the pulsar wind.

In Figures 9-11, we discuss the dependency of the light curve on (i) the eccentricity and (ii) the position of the INFC/SUPC rel-

ative to the periastron. The eccentricity introduces a variation of the distance to the apex from the pulsar along the orbital phase, and the periastron (or apastron) is defined at the position where the distance between the pulsar and companion star is the shortest (or the longest).

In Figure 9, to investigate the dependency of the eccentricity, we assume that the position of periastron and apastron are coincide with the SUPC and INFC, respectively, and we choose  $\Phi_{peri} = \Phi_{SUPC} = 0$  and  $\Phi_{apa} = \Phi_{INFC} = 0.5$ . From Figures 9, we see that as the eccentricity increases, the double peak structure disappears and the peak at periastron/SUPC becomes sharper. This can be understood because for a larger eccentricity, the distance between the pulsar and companion star at the periastron is shorter and hence the density of soft-photon at the emission region is larger. As Figure 3 shows, with increase of the eccentricity, (i) the travel distance at the SUPC decreases and (ii) the variation of the amplitude along the orbit increases. Although this effect of the travel lengths tends to decrease the observed flux at the SUPC, it is overcome by the effect of the increase in the soft-photon density at the emission region. As a result, the model light curve has a more prominent peak at SUPC for larger eccentricity. We conclude therefore that the effect of the travel distance is more important for the pulsar binary system with a lower eccentricity.

In Figure 10, we consider the opposite case of Figure 9, namely, we assume the position of the periastron and apastron at  $\Phi_{peri} = \Phi_{INFC} = 0$  and  $\Phi_{apa} = \Phi_{SUPC} = 0.5$ , respectively. In this case, we can see local minima located at SUPC and INFC for all eccentricity. The local minimum at apastron/SUPC is created as a result of the minimum of the soft-photon density at the emission region, and the minimum at periastron/INFC is produced as a result of the minimum of the collision angle.

Since 4FGL J1405.4-6119 likely shows the double peak structure in the GeV light curve, its position of the INFC/SUPC relative to periastron/apastron could be similar to the case of Figure 10. In Figure 11, therefore, we summarize how the shape of the light curve depends on the periastron/apastron relative to the SUPC/INFC with the eccentricity  $e = 0.4$  and the system inclination angle  $\alpha = 60^\circ$ . In the top-left panel, we represent the double peak light curve with the geometry  $\Phi_{INFC} = \Phi_{peri} = 0$ . Then we shift the position of the INFC to  $\Phi_{INFC} = 0.05$  (top-right),  $0.15$  (bottom-left) and  $0.25$  (bottom-right), respectively; the position of the periastron and apastron are fixed at  $\Phi_{peri} = 0$  and  $\Phi_{apa} = 0.5$ , respectively. As the position of the INFC, at which the calculated flux is minimum, is shifted away from the periastron (in other words, the SUPC is shifted toward the periastron), the flux minimum also shifts, and the dip appeared at SUPC becomes shallower. The calculated light curve is eventually described by the single peak.



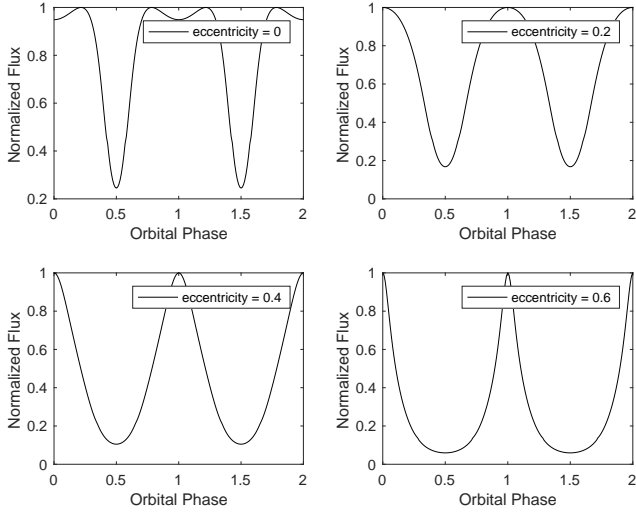


**Figure 9.** Dependency of the orbital modulation of ICS emission from unshocked pulsar wind with the eccentricity. The result is for inclination angle is 60 degrees. The INFC and SUPC happen at  $\Phi_{INFC} = 0.5$  and  $\Phi_{SUPC} = 0$ , respectively.

We created the light curve with the various system parameters to examine allowed range of the parameters that produce the double peak structure. For the eccentricity  $e = 0.4$  and the inclination angle  $\alpha = 60^\circ$  of Figure 11, for example, we find that the allowed range of the position of INFC that create the double peak structure in the light curve is  $|\delta\Phi_{INFC}| < 0.05$  measured from the periastron. We note that although the allowed range if  $\Phi_{INFC}$  is within 10% of the orbital phase measured in time, it corresponds to  $\leq 50^\circ$  in the true anomaly for the eccentricity  $e = 0.4$ . Hence, such a viewing geometry will be not uncommon. We can find that the allowed range of the  $\Phi_{INFC}$  in true anomaly is not sensitive to the eccentricity, but a larger eccentricity creates double peaks with a smaller phase separation, as indicated in Figure 10. As decrease of the system inclination angle from  $\alpha = 60^\circ$ , the double peak structure transits to the single peak. With the eccentricity  $e = 0.4$  and  $\Phi_{INC} = 0.05$  (tot-right panel in Figure 10, for example, the lower limit of the inclination angle to create the double peak structure is  $\sim 40^\circ$ .

## 4.2 Application to LMC P3

To explain the observed flux level, Corbet et al. (2016) suggests that the spin-down power of the pulsar is about  $L_{sd} = 4.3 \times 10^{36} \text{ erg s}^{-1}$ . In this study, we assume  $L_{sd} = 6 \times 10^{36} \text{ erg s}^{-1}$ . To estimate the magnetic field at the shock, we apply  $\sigma = 0.003$ , which is measured for the Crab pulsar, of the magnetization parameter at the termination shock. With  $\sigma = 0.003$ , the magnetic field strength at the shock is of the order of 1G. We also assume  $R_c = 14.5R_\odot$  for the radius of companion star to estimate the angular size of the companion star,  $\theta_c$ , in the equation of (3), and assume  $T_c \sim 2.5 \times 10^4 \text{ K}$  for the temperature of the companion star. Tables 1 and 2 summarize the parameters of the system applied in this study. The pulsar goes around the O star in the orbit shown in figure 1.

### 4.2.1 GeV light curve

The current model assumes that the GeV emission modulating with the orbital phase is produced by the ICS of the unshocked pulsar wind off the stellar photon. The GeV emission from LMC P3

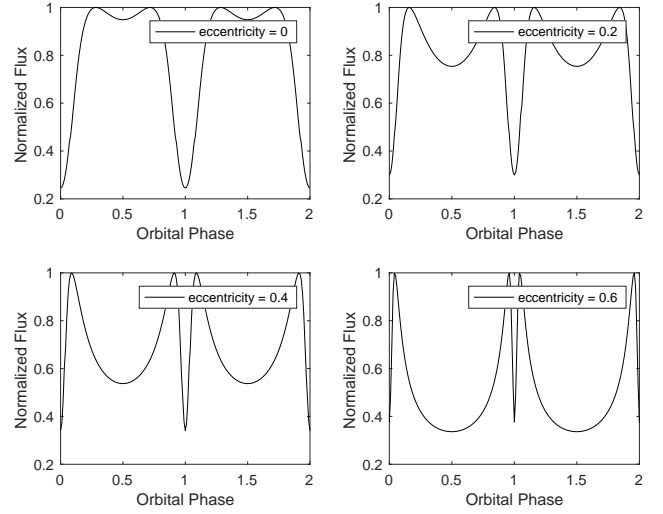


**Figure 10.** Dependency of the orbital modulation of ICS emission from unshocked pulsar wind with the eccentricity. The result is for the system inclination angle  $\alpha = 60^\circ$ . The INFC and SUPC happen at  $\Phi_{INFC} = 0$  and  $\Phi_{SUPC} = 0.5$ .

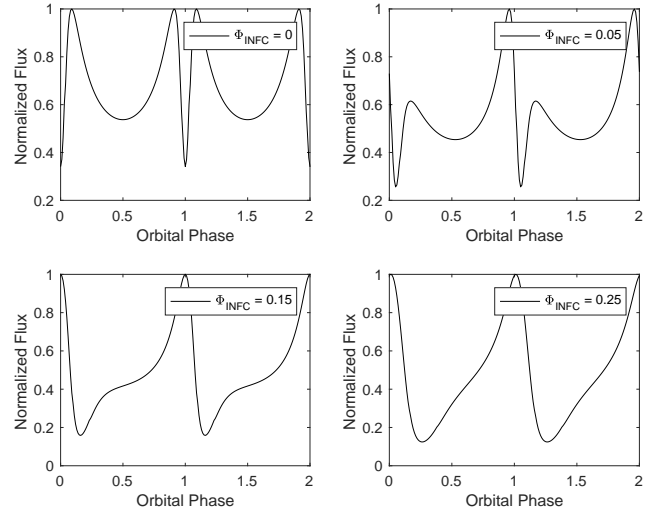


**Figure 11.** Dependency of the orbital modulation of ICS emission from unshocked pulsar wind with the position of INFC. The result is for eccentricity is 0.4. The position of INFC and SUPC are  $(\Phi_{INFC}, \Phi_{SUPC}) = (0, 0.5)$  for upper-left panel,  $(0.05, 0.73)$  for upper-right panel,  $(0.15, 0.89)$  for lower-left panel and  $(0.25, 0.94)$ , respectively. The periastron is located at  $\Phi_{peri} = 0.0$  in each panel.

gamma-ray binary shows a broad asymmetric peak structure and probably has a double peak structure in the light curve. As we discussed above, the shape of the light curve depends on the system parameters,  $\eta$ ,  $\alpha$  and  $e$ . To fit the observed radial velocity curve, Corbet et al. (2016) obtain the SUPC at the  $\Phi_{SUPC} \sim 0.8 - 0.9$ , where the phase zero is defined at MJD 57,410.25. van Soelen et al. (2019) refine the orbit parameter with a more detailed optical observation. With  $\Phi_{orb} = 0$  at MJD 57,410.25, the periastron, INFC and SUPC occur at  $\Phi_{peri} = 0.13$ ,  $\Phi_{INFC} = 0.24$  and  $\Phi_{SUPC} = 0.98$ , respectively. The eccentricity is measured as  $e \sim 0.4$ , and the measured mass function implies that the inclination angle,  $\alpha$ , is between  $\alpha \sim 40^\circ$  and  $60^\circ$  with  $1.4M_\odot$  for the mass of the compact object and  $25 - 40M_\odot$  for the mass of companion star.

Figure 12 compares the light curves observed by *Fermi*-LAT ( $> 100\text{MeV}$ ) with the calculated light curve with using the systems parameters obtained by [van Soelen et al. \(2019\)](#); we assume the momentum ratio  $\eta = 0.03$  and the inclination angle  $\alpha \sim 40^\circ$  which is lower limit for the neutron star mass  $1.4M_\odot$  given by [van Soelen et al. \(2019\)](#). The dotted line and solid line in the figure are the calculated light curve without and with the effect of the travel distance of the unshocked pulsar wind, respectively. We find in the figure that the modulation in the calculated light curve ignoring the effect of the travel distance becomes significantly larger than that of the observations. We also see that the width of the peak located at the SUPC is narrower than the observation. By taking account for the effect of the travel distance (solid line in the figure), we can see in the figure that the amplitude of the calculated light curve (solid line) is reduced and it is more consistent with the observation. With the suggested orbital parameters, therefore, the effect of the travel distance of the unshocked pulsar wind is important to explain the observed orbital modulation, proving that the GeV emission is originated from the unshocked pulsar wind.

As the solid line in Figure 12 shows, the model light curve with the inclination angle  $\alpha = 40^\circ$  would have a peak narrower than the observed one and the model flux at  $\Phi_{orb} \sim 0.8$  would be significantly deviated from the observation, although the uncertainties of the error are large. We therefore calculate the model light curve with different inclination angle, and we find that the model light curve with a different inclination angle does not improve this feature. In Figure 12, for example, we present the model light curve with the inclination angle  $\alpha = 30^\circ$ , for which the mass of the compact object is slightly larger than  $1.4M_\odot$  with  $25 - 40M_\odot$  of a companion star. Due to the observed uncertainty of orbital parameters, we shift the position of the SUPC, periastron and INFC to  $\Phi_{orb} = 0.98, 0.03$  and  $0.24$ , respectively, which are still in the range suggested by [van Soelen et al. \(2019\)](#). Figure 13 compares the model light curve with the observations. Compared with the model light curves (solid and dashed lines) in Figure 12, the position of peak is shifted because of the applied positions of SUPC and periastron. The feature of slow rising and rapid decreasing of the peak shape and the peak width would be more consistent with the observations within the range of the errors. We note that current model does not expect the double peak structure of the light curve, as seen in Figure 11, with the system parameters of the LMC P3, because we observe the system from the direction far from the periastron.

#### 4.2.2 X-ray/TeV light curves

We assume that the synchrotron emission and ICS process of the shocked pulsar wind particles produce the X-ray and TeV gamma-ray, respectively, of LMC P3. Using the system parameters obtained from the fitting of the GeV light curve in Figure 13 (Table 2), we calculate the shock emission.

Figure 14 compares the observed X-ray light curves with calculated X-ray light curve. In the current model, the orbital modulation of the X-ray is caused by (i) the Doppler boosting process ([Dubus et al. 2010](#)) and (ii) variation of the shock distance from the pulsar/companion star, which causes the variation of the cooling timescale along the orbit ([Khangulyan et al. 2007](#); [Takata & Taam 2009](#)). In the current emission model, we find that the second effect on the orbital modulation cannot reproduce the observed amplitude of the orbital variation in the X-ray bands, and therefore we expect that the Doppler boosting effect mainly causes the observed orbital variation. With the Doppler boosting effect, the maximum and min-

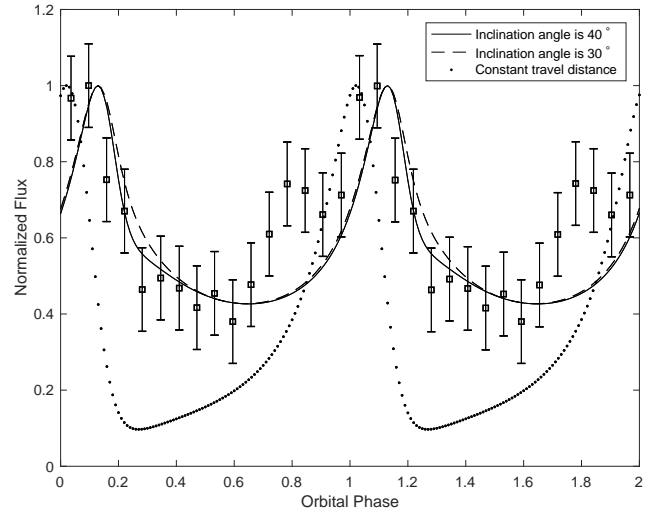


**Figure 12.** GeV light curve of LMC P3. The lines are model light curve with the system parameters suggested in the [van Soelen et al. 2019](#). The periastron, INFC and SUPC are  $\Phi_{peri} = 0.13, \Phi_{INFC} = 0.24$  and  $\Phi_{SUPC} = 0.98$ , respectively. And the inclination angle is  $40^\circ$  for solid line and dash line for  $30^\circ$ . The data are taken from [Corbet et al. 2016](#)

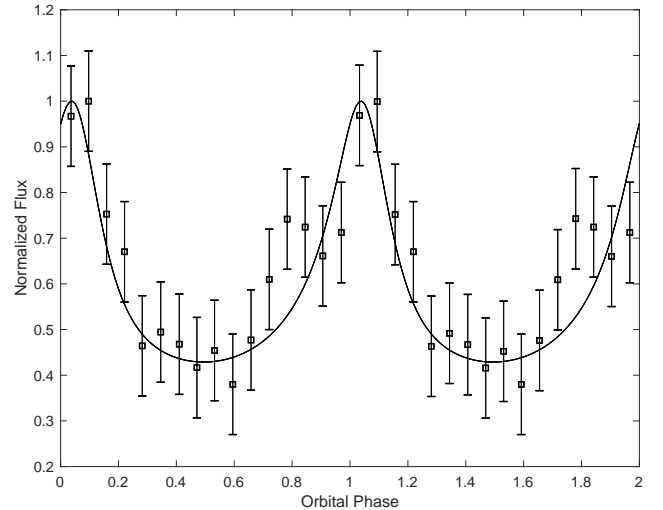


**Figure 13.** GeV light curve of LMC P3. The solid line is model light curve with the system parameters presented in the Table 1. The data are taken from [Corbet et al. 2016](#)

imum intensity of the X-ray emission tend to appear at INFC and SUPC, respectively. To explain the amplitude of the observed modulation, we assume the Lorentz factor of the shocked pulsar wind in the value of  $\Gamma_{sw} \sim 1.08$  ( $\beta_{sw} \sim 0.35$ ).

Figure 15 presents the predicted TeV light curve. In the TeV energy bands, the orbital modulation is caused by (i) the Doppler boosting, (ii) the variation of the soft-photon field at the emission region and (iii) the absorption owing to the pair-creation process. With the assumed system parameters in Table 1 and 2, we find that optical depth of 1TeV photons that are traveling toward the observer is less than unity for whole orbit (Figure 16). With the inclination angle  $\alpha = 30^\circ$ , the effect of the collision angle on the orbital variation is less important, and therefore the Doppler boosting effect dominates in the orbital modulation of the model light curve. Our model predicts that the light curve has a peak (or minimum) intensity around the INFC (or SUPC). [HESS Collaboration et al.](#)

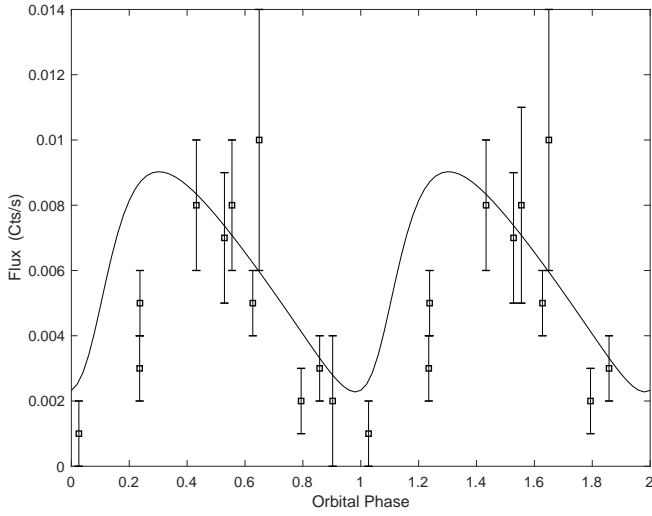


**Figure 14.** X-ray light curve of LMC P3. The solid line is model light curve with the system parameters presented in the Table 1. The data are taken from Corbet et al. 2016

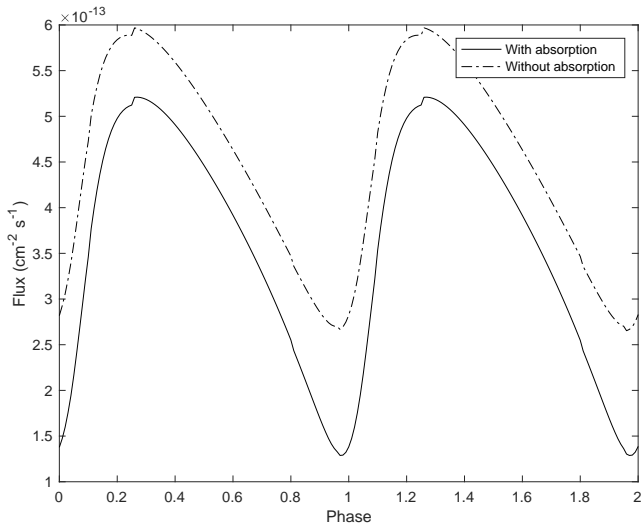


**Figure 15.** The predicted light curve in 1-100 TeV energy bands with the system parameters of Tables 1 and 2. The solid line and dashed line represent the model light curves with absorption and without absorption respectively.

(2018) found a significant TeV emission around the INFC, which is consistent with the current model. Since the TeV emission at most of orbital phase has not been confirmed by the current observation, we do not pursue a detail comparison between the model and observed light curves.

#### 4.2.3 Broadband spectrum

Figure 17 compares between the calculated and observed spectra averaged over the whole orbit. In the current model, the ICS of the unshocked pulsar wind (dotted-dashed line) explains the observed spectrum in  $10^{8-9}$  eV energy bands, while the synchrotron radiation and ICS process of the shocked pulsar wind (solid line) explain the observed X-ray and TeV emission, respectively.

It has been discussed the emission from the secondary pairs

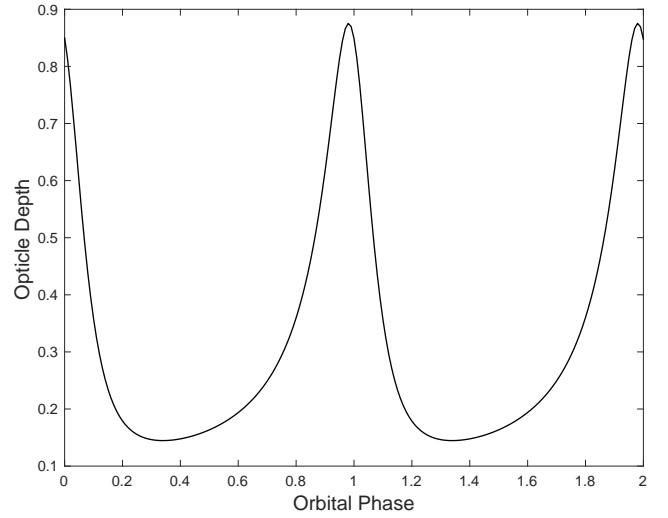


**Figure 16.** The orbital variation of optical depth along the line of sight for 1 TeV photon with the system parameters of Tables 1 and 2.

created at the stellar wind region by the photon-photon annihilation process (Bednarek 1997; Sierpowska-Bartosik & Bednarek 2008; Sierpowska-Bartosik & Torres 2007; Cerutti et al. 2010). As shown in Figure 6, the photon with an energy larger than  $\sim 10^{10}$  eV may be converted into the pairs, and therefore the Lorentz factor of the secondary are typically in the range of  $\sim 10^5 - 10^7$ . To estimate the synchrotron emission of the secondary pairs created at the stellar wind region, we assume that the magnetic field where the secondary emission occurs is dominated by O star's magnetic field and we apply a simple power law form  $B(R) = B_c(R/R_c)^{-m}$  with  $B_c$  being the stellar magnetic field and  $R$  distance to the emission region from the star. The stellar magnetic field of the high mass main-sequence star can be  $B_c \sim 10^{2-3}$  G (Walder et al. 2012). With a typical value  $m = 2 - 3$ , we can see that the synchrotron emission of the second pairs is stronger than ICS process only at near the companion star. In the current model, therefore, the synchrotron emission from the secondary is negligible in the observed emissions. To discuss the ICS process, we assume that the secondary pairs created in the stellar wind region are quickly isotropized and we calculate the ICS process with a constant soft-photon field during the crossing timescale  $D/c$ . In Figure 17, the dotted line represents the contribution of the emission from the secondary pairs.

#### 4.3 Application to 4FGL J1405.4-6119

4FGL J1405.4-6119 is the new gamma-ray binary discovered by *Fermi* (Corbet et al. 2019). The GeV light curve measured by *Fermi* would show a double peak structure with the small peak and sharp strong peak (Figure 18). The strong peak is probably shifted from the peak of the X-ray (Corbet et al. 2019), which is similar to LMC P3 and LS 5039. We therefore expect that GeV emission from the source is originated from the ICS of the unshocked pulsar wind.

The system parameters have not been determined yet. In this paper, therefore, we assume the eccentricity  $e = 0.4$ , the momentum ratio  $= 0.03$  and the temperature of the companion star  $T_c \sim 2.5 \times 10^4$  K, which were applied for the case of LMC P3. The expected phase of the periastron, SUPC and INFC are determined by the fitting of the GeV light curve, as shown in Figure 18. As we discussed in section 4.1, the current model predicts the double

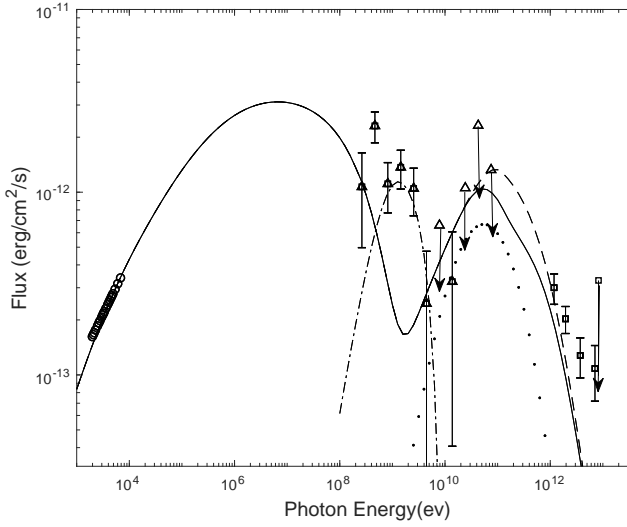


**Figure 17.** The solid line is spectra of shock emission with photon-photon absorption. The dash line is the spectrum without the absorption. Dash-dot line is PW emission and the dot line is secondary emission. X-ray data and TeV data are taken from Corbet et al. 2016 and from Komin 2017, respectively.

peak structure if the SUPC happens at around apastron, namely, we observe the system from the direction of the periastron. In Figure 18, we fit the *Fermi* data with  $\Phi_{\text{peri}} = 0.1$ ,  $\Phi_{\text{INFC}} = 0.18$  and  $\Phi_{\text{SUPC}} = 0.91$ ; the true anomalies of INFC and SUPC measured from the periastron are  $65^\circ$  and  $245^\circ$ , respectively. Our model predicts that the sharp peak is located at around the periastron, and there is a local minimum at the phase between the apastron and SUPC. The requirement for reproducing the double peak structure that we observe the system from the direction of the periastron is not sensitive to the eccentricity and the system inclination angle. The future observations for the system parameter will be compared with the model prediction.

## 5 SUMMARY

We have studied the GeV emission from the gamma-ray binary systems composed of young pulsar and O-type main-sequence star. In our model, the GeV emission is originated from the ICS process of the unshocked pulsar wind off the soft-photons from the companion star. The unshocked pulsar wind is stopped by the intra-binary shock and the travel distance of the unshocked wind that moves toward the observer depends on the orbital phase. In this paper, we studied how the effect of the travel distance affects to the orbital modulation of the observed GeV emission.

Comparing with the model light curve in which the constant travel distance along the orbital phase is assumed, the effect of the travel distance tends to create a small dip around the SUPC, where the travel distance is the minimum. In addition, the effect makes the peak width wider. In a real situation, the effect of the travel distance compensates with the effect of anisotropic soft-photon field, and this effect is more prominent for the binary system with a lower eccentricity and a stellar wind being much stronger than the pulsar wind. For the system with the higher eccentricity, the shape of the

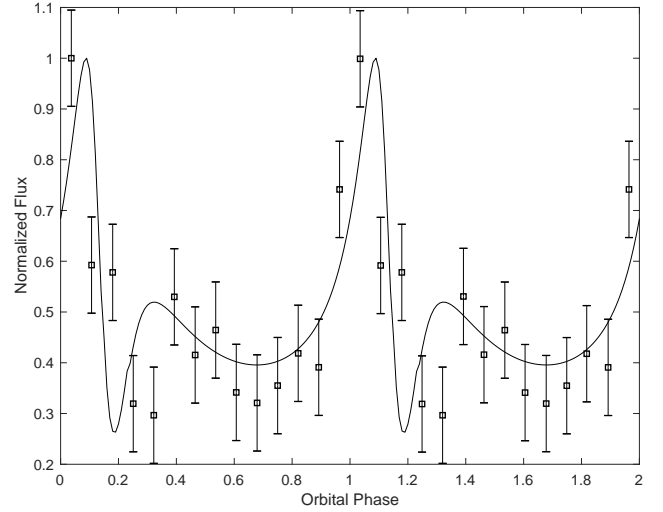


**Figure 18.** GeV light curve of 4FGL J1405.4-6119. The solid line is model light curve with the orbit parameters  $\eta = 0.03$ ,  $\alpha = 60^\circ$  and  $e = 0.4$ . We assume  $\Phi_{\text{peri}} = 0.1$ ,  $\Phi_{\text{INFC}} = 0.18$  and  $\Phi_{\text{SUPC}} = 0.91$ , and apply the parameters of the companion star in Table 1. The data points of the *Fermi*-LAT are taken from Corbet et al. 2019.

light curve and the peak position are mainly affected by the effect of the anisotropic soft-photon field.

We apply the our model to two gamma-ray binaries, LMC P3 and 4FGL J1405.4-6119 that were recently discovered by *Fermi*-LAT. Applying the system parameters of LMC P3 suggested by van Soelen et al. (2019), our model light curve with the effect of the travel distance would be consistent with the observed GeV light curve. In particular, we found that the observed amplitude of the modulation and width of the peak can be described as a result of the effect of the travel distance. We also calculated the X-ray/TeV emission from the shocked pulsar wind and found that the Doppler boosting effect is more important to explain the observed X-ray modulation with the suggested system parameters. Within the current model, we suggest that the observed double peak structure in the GeV light curve of 4FGL J1405.4-6119 is owing to the anisotropic soft-photon field and we predict that the system is viewed from the direction close to the periastron. Future observations for the system parameters will be compared with the our prediction to constrain the GeV emission process.

We wish to express our thanks to the referee for detailed comments to improved the paper. We also thank to Prof. K.S. Cheng and Dr. A.M. Chen for useful discussion for the gamma-ray binaries. This work has made use of data supplied by the Fermi Science Support Center and the software supplied by the Fermipy Developers. H.X.X. and J.T. are supported by NSFC grants of the Chinese Government under 11573010, 11661161010, U1631103 and U1838102. T.Q.W. is supported by the NSFC under 11903017 and 11547029.

## REFERENCES

- Abdo A. A., et al., 2009, *ApJ*, **706**, L56
- Abdo A. A., et al., 2011, *ApJ*, **736**, L11
- Abeysekara A. U., et al., 2018, *ApJ*, **867**, L19
- Ackermann M., et al., 2016, *A&A*, **586**, A71
- Aharonian F., et al., 2005, *A&A*, **442**, 1
- Aharonian F., et al., 2006, *A&A*, **460**, 743
- Albert J., et al., 2006, *Science*, **312**, 1771



- Aliu E., et al., 2013, *ApJ*, **779**, 88
- An H., Romani R. W., 2017, *ApJ*, **838**, 145
- An H., et al., 2015, *ApJ*, **806**, 166
- Ball L., Kirk J. G., 2000, *Astroparticle Physics*, **12**, 335
- Bednarek W., 1997, *A&A*, **322**, 523
- Bogovalov S. V., Khangulyan D. V., Koldoba A. V., Ustyugova G. V., Aharonian F. A., 2008, *MNRAS*, **387**, 63
- Bogovalov S. V., Khangulyan D., Koldoba A., Ustyugova G. V., Aharonian F., 2019, *MNRAS*, **490**, 3601
- Bosch-Ramon V., Barkov M. V., Khangulyan D., Perucho M., 2012, *A&A*, **544**, A59
- Canto J., Raga A. C., Wilkin F. P., 1996, *ApJ*, **469**, 729
- Cerutti B., Dubus G., Henri G., 2010, in Martí J., Luque-Escamilla P. L., Combi J. A., eds, *Astronomical Society of the Pacific Conference Series* Vol. 422, *High Energy Phenomena in Massive Stars*. p. 41
- Chang Z., Zhang S., Ji L., Chen Y. P., Kretschmar P., Kuulkers E., Collmar W., Liu C. Z., 2016, *MNRAS*, **463**, 495
- Chen A. M., Takata J., Yi S. X., Yu Y. W., Cheng K. S., 2019, *A&A*, **627**, A87
- Chernyakova M., Neronov A., Aharonian F., Uchiyama Y., Takahashi T., 2009, *MNRAS*, **397**, 2123
- Chernyakova M., et al., 2015, *MNRAS*, **454**, 1358
- Cominsky L. R., 1994, Technical report, ROSAT observations of the binary Be-star and radio pulsar PSR1259-63
- Corbet R. H. D., et al., 2016, *ApJ*, **829**, 105
- Corbet R. H. D., et al., 2019, arXiv e-prints, [p. arXiv:1908.10764](https://arxiv.org/abs/1908.10764)
- Davies R. D., Elliott K. H., Meaburn J., 1976, *MmRAS*, **81**, 89
- Dubus G., 2013, *A&A Rev.*, **21**, 64
- Dubus G., Cerutti B., Henri G., 2010, *A&A*, **516**, A18
- Gould R. J., Schröder G. P., 1967, *Physical Review*, **155**, 1404
- H. E. S. S. Collaboration et al., 2012, *A&A*, **541**, A5
- HESS Collaboration et al., 2018, *A&A*, **610**, L17
- Hibschman J. A., Arons J., 2001a, *ApJ*, **554**, 624
- Hibschman J. A., Arons J., 2001b, *ApJ*, **560**, 871
- Hinton J. A., et al., 2009, *ApJ*, **690**, L101
- Ho W. C. G., Ng C. Y., Lyne A. G., Stappers B. W., Coe M. J., Halpern J. P., Johnson T. J., Steele I. A., 2017, *MNRAS*, **464**, 1211
- Jauch J. M., Rohrlich F., 1976, *The theory of photons and electrons. The relativistic quantum field theory of charged particles with spin one-half*
- Johnston S., Manchester R. N., Lyne A. G., Bailes M., Kaspi V. M., Qiao G., D'Amico N., 1992, *ApJ*, **387**, L37
- Kapala M., Bulik T., Rudak B., Dubus G., Lyczek M., 2010, in *25th Texas Symposium on Relativistic Astrophysics*. p. 193
- Kennel C. F., Coroniti F. V., 1984a, *ApJ*, **283**, 694
- Kennel C. F., Coroniti F. V., 1984b, *ApJ*, **283**, 710
- Khangulyan D., Hnatic S., Aharonian F., 2007, *Ap&SS*, **309**, 261
- Khangulyan D., Aharonian F., Bosch-Ramon V., 2008, *MNRAS*, **383**, 467
- Komin N., 2017, in *5th Annual Conference on High Energy Astrophysics in Southern Africa*. p. 33
- Li J., Torres D. F., Cheng K. S., de Oña Wilhelmi E., Kretschmar P., Hou X., Takata J., 2017, *ApJ*, **846**, 169
- Long K. S., Helfand D. J., Grabelsky D. A., 1981, *ApJ*, **248**, 925
- Lyne A. G., Stappers B. W., Keith M. J., Ray P. S., Kerr M., Camilo F., Johnson T. J., 2015, *MNRAS*, **451**, 581
- Macri L. M., Stanek K. Z., Bersier D., Greenhill L. J., Reid M. J., 2006, *ApJ*, **652**, 1133
- Mariaud C., Bordas P., Aharonian F., Dubus G., Böttcher M., de Naurois M., Romoli C., Zabalza V., 2015, in *34th International Cosmic Ray Conference (ICRC2015)*. p. 885
- Martí-Devesa G., Reimer O., 2020, arXiv e-prints, [p. arXiv:2001.02701](https://arxiv.org/abs/2001.02701)
- Moldón J., Ribó M., Paredes J. M., 2012, *A&A*, **548**, A103
- Moritani Y., Kawano T., Chimasu S., Kawachi A., Takahashi H., Takata J., Carciofi A. C., 2018, *PASJ*, **70**, 61
- Pietrzyński G., et al., 2013, in Pavlovski K., Tkachenko A., Torres G., eds, Vol. 64, *EAS Publications Series*. pp 305–307, [doi:10.1051/eas/1364042](https://doi.org/10.1051/eas/1364042)
- Puls J., et al., 1996, *A&A*, **305**, 171
- Seward F. D., Charles P. A., Foster D. L., Dickel J. R., Romero P. S., Edwards Z. I., Perry M., Williams R. M., 2012, *ApJ*, **759**, 123
- Sierpowska-Bartosik A., Bednarek W., 2008, *MNRAS*, **385**, 2279
- Sierpowska-Bartosik A., Torres D. F., 2007, *ApJ*, **671**, L145
- Sierpowska-Bartosik A., Torres D. F., 2008, in Aharonian F. A., Hofmann W., Rieger F., eds, Vol. 1085, *American Institute of Physics Conference Series*. pp 253–256, [doi:10.1063/1.3076653](https://doi.org/10.1063/1.3076653)
- Takahashi T., et al., 2009, *ApJ*, **697**, 592
- Takata J., Taam R. E., 2009, *ApJ*, **702**, 100
- Takata J., Leung G. C. K., Tam P. H. T., Kong A. K. H., Hui C. Y., Cheng K. S., 2014, *ApJ*, **790**, 18
- Takata J., Tam P. H. T., Ng C. W., Li K. L., Kong A. K. H., Hui C. Y., Cheng K. S., 2017, *ApJ*, **836**, 241
- Tam P. H. T., Huang R. H. H., Takata J., Hui C. Y., Kong A. K. H., Cheng K. S., 2011, *ApJ*, **736**, L10
- Tam P. H. T., He X. B., Pal P. S., Cui Y., 2018, *ApJ*, **862**, 165
- Tam P.-H. T., et al., 2020, arXiv e-prints, [p. arXiv:2001.07138](https://arxiv.org/abs/2001.07138)
- Tang Q.-W., 2018, *Ap&SS*, **363**, 25
- Tang Q.-W., Peng F.-K., Liu R.-Y., Tam P.-H. T., Wang X.-Y., 2017, *ApJ*, **843**, 42
- Tavani M., Arons J., 1997, *ApJ*, **477**, 439
- Timokhin A. N., Harding A. K., 2015, *ApJ*, **810**, 144
- Timokhin A. N., Harding A. K., 2019, *ApJ*, **871**, 12
- Torres D. F., 2011, *Astrophysics and Space Science Proceedings*, **21**, 531
- Walder R., Folini D., Meynet G., 2012, *Space Sci. Rev.*, **166**, 145
- Wood M., Caputo R., Charles E., Di Mauro M., Magill J., Perkins J. S., Fermi-LAT Collaboration 2017, in *35th International Cosmic Ray Conference (ICRC2017)*. p. 824 ([arXiv:1707.09551](https://arxiv.org/abs/1707.09551))
- Yamaguchi M. S., Takahara F., 2012, *ApJ*, **761**, 146
- Zabalza V., Bosch-Ramon V., Aharonian F., Khangulyan D., 2013, *A&A*, **551**, A17
- de Grijs R., Wicker J. E., Bono G., 2014, *AJ*, **147**, 122
- van Soelen B., Komin N., Kniazev A., Väisänen P., 2019, *MNRAS*, **484**, 4347